Article

Controlled Fabrication of Flower-Shaped Au−Cu Nanostructures Using a Deep Eutectic Solvent and Their Performance in Surface-Enhanced Raman Scattering-Based Molecular Sensing

Siva Kumar-Krishnan,* Rodrigo Esparza, and Umapada Pal*

Cite This: *ACS Omega* 2020, 5, 3699−3708

Read Online

ACCESS | 📊 Metrics & More | 📰 Article Recommendations | 🆂🆸 Supporting Information

ABSTRACT: Controlled synthesis of anisotropic bimetallic nanostructures with tunable morphology is of great current interest for their applications in surface-enhanced Raman scattering (SERS), plasmonics, and catalysis. Despite huge effort that has been devoted so far, fabrication of bimetallic nanostructures with controlled morphology and size remained to be a great challenge, especially when their shapes are anisotropic. Here, we report a facile, one-step synthetic approach for the fabrication of anisotropic bimetallic gold−copper nanostructures (Au−Cu NSs) of the 200−300 nm size range, using choline chloride/urea (ChCl/urea)-based deep eutectic solvent (DES) as the soft template. A concentration of the $CuCl_2$ precursor in the reaction mixture was found to impact the reduction kinetics of the metal ions, directly affecting the final morphology of the Au−Cu nanostructures and elemental distributions in them. The fabricated anisotropic Au−Cu NSs revealed a high SERS signal for crystal violet (CV) molecules adsorbed at their surfaces, with the signal enhancement factor as high as 0.21×10^6 and capacity of detecting CV molecules of concentrations as low as 10^{-10} M in their aqueous solutions. The growth mechanism of the anisotropic bimetallic nanostructures in DES and their SERS performance has been discussed. The simple DES-assisted synthesis strategy presented in this work can be adopted for large-scale nonaqueous fabrication of other bimetallic nanostructures in a quite "greener" way.
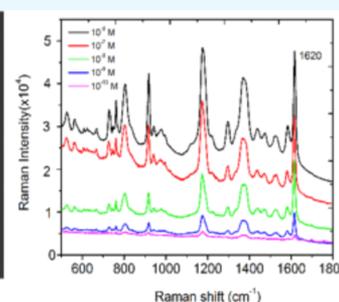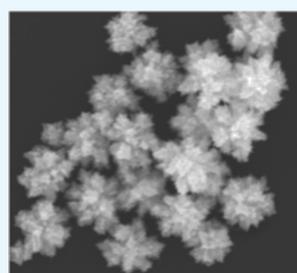
1. INTRODUCTION

Bimetallic plasmonic nanostructures have attracted significant research interest in recent years because of exceptional optical properties derived from their size, shape, and composition.[1] Localized surface plasmon resonance (LSPR) generated from the collective oscillation of quasi-free electrons of the metallic nanostructures under external electromagnetic excitation[2] has been exploited to utilize them in different technological applications such as nonlinear optical devices,[2] theranautics,[3] photovoltaic devices,[4] biosensing,[5,6] photocatalysis,[7] and medical diagnosis.[8,9] On the other hand, exploiting the phenomenon that plasmonic nanostructures confine incident electromagnetic field near their surfaces (near-field enhancement),[3] they have been utilized as substrates for surface-enhanced Raman scattering (SERS)-based molecular sensing.[14,15] As both the far-field (LSPR) and near-field behaviors of plasmonic nanostructures depend strongly on their geometrical features (e.g., size, shape, and surface texture) and interparticle distance in their assemblies,[10−12] fabrication of plasmonic nanostructures with precise control over their morphology is one of the vital issues that should be resolved before their technology-specific applications.

Nanostructures of noble metals such as silver,[13,14] gold,[15] and copper[16] have drawn much attention in recent times

because of their intense LSPR, tunable from the visible to near-infrared (NIR) region, and near-field enhancements. In particular, there is a growing interest in developing different bimetallic nanostructures with a controlled size and shape, such as core−shell structures with thin (few atoms) plasmonic shells,[17] porous nanostructures with built-in "hot spots",[18,19] dendritic structures,[20,21] and three-dimensional (3D) hierarchical nanostructured substrates[22,23] with controlled interparticle spacing[24] in order to create abundant "hot spots" to accomplish stable and enhanced SERS performance. Among the plasmonic nanostructures utilized for SERS applications, 3D-branched nanostructures have drawn special attention because of their anisotropic shapes, which can provide a large accessible surface area with abundant exposed active sites, capable of producing far-field and near-field optical responses quite different from that of common spherical plasmonic nanoparticles.[22,25] The added advantage of using such 3D nanostructures in molecular sensing is that the probe
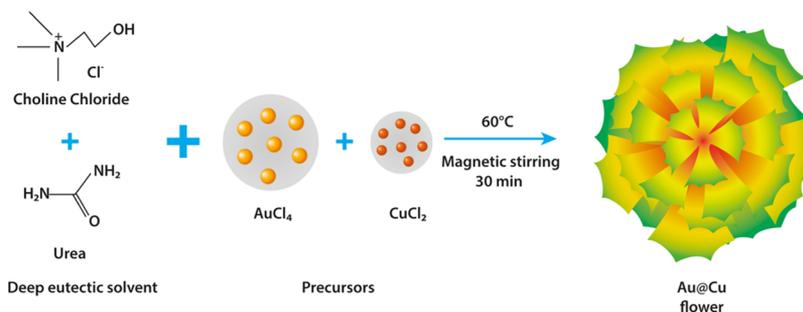
Scheme 1. Schematic Representation of Synthesis Steps Used for the Fabrication of Au−Cu Nanostructures in DES

molecules or analytes can diffuse effectively inside their nanocavities, which significantly increases the adhesion of analyte molecules at their surfaces, enhancing the overall SERS signal.[26]

Over the last decade, anisotropic Au NPs have been extensively investigated as effective SERS substrates because of their geometry-dependent tunable optical properties, easy surface engineering, and structural stability.[27−29] Recently, Au−Cu bimetallic nanostructures have demonstrated to exhibit interesting optical properties because of strong intermediate bonding of Cu, good miscibility over a wide composition range, and composition-dependent tunable LSPR properties.[30−32] Furthermore, the large lattice mismatch between Au and Cu induces anisotropic growth, favoring the formation of highly branched nanostructures with significant strain in their surfaces, which also affects their performance in SERS-based spectroscopic applications.[33−35] Numerous synthetic approaches have been exploited for the fabrication of Au−Cu bimetallic nanostructures with controlled size, composition, and geometry.[36−39] However, there exist only a very few eco-friendly or green synthesis pathways capable of producing metallic nanostructures of controlled morphology. In this context, deep eutectic solvents (DESs) have emerged as cost-effective, nonaqueous green mediums for controlled synthesis of metallic and semiconducting nanostructures.[40] DES are nontoxic, biodegradable, and environmental friendly ionic liquid analogues, usually formed by complexion of quaternary ammonium salt and hydrogen bond donors such as amides, carboxylic acids, and polyols, use of which was first reported by Abbott et al. in 2003.[41] In addition, extended hydrogen-bonded structures of DES serve as the soft template for controlled anisotropic growth of a great variety of nanostructures.[42,43] Since the utilization of DES for synthesizing anisotropic Au nanostructures reported by Liao et al.[44] in 2008, this approach has been extended for fabricating metallic,[45] metal oxides,[46−48] and dielectric,[49] nanostructures. However, DES-assisted fabrication of uniform bimetallic Au−Cu nanostructures of tailored geometries remained a challenge.

Herein, we demonstrate a novel, ecofriendly synthetic strategy for the fabrication of uniform Au−Cu bimetallic nanostructures of different geometries using ChCl/urea-based DES, for their utilization as efficient SERS substrates. Au−Cu nanostructures of different morphologies were obtained by varying the molar ratio of Au and Cu precursors under similar reaction conditions. SERS activity of the fabricated nanostructures was examined by adsorbing crystal violet (CV) as a probe molecule and exciting by a 633 nm laser beam. The branched flower-shaped Au−Cu nanostructures exhibit enhanced SERS activity for the detection of CV molecules, with a detection limit as low as 10^{-10} M. SERS activities of the flower-shaped

Au−Cu nanostructures has been compared with Au−Cu nanostructures of other morphologies fabricated by the same DES-assisted synthesis.

2. RESULTS AND DISCUSSION

2.1. Synthesis and Structural Characterization of Au−Cu Nanostructures. The branched Au−Cu nanostructures were synthesized by reducing Au^{3+} and Cu^{2+} ions using L-ascorbic acid (AA) as the reducing agent and DES as shape-directing, nonaqueous "soft template" for their controlled anisotropic growth (Scheme 1). The flower-like nanostructures were formed only for the concentrations of the Cu^{2+} precursor in the reaction mixture $Au^{3+}-Cu^{2+} > 1{:}0.3$. It is well known that both Au and Cu metals possess a face-centered cubic (fcc) crystalline structure, with about 11.4% lattice mismatch (lattice constants of Au and Cu are 0.4079 and 0.3615 nm, respectively).[50] While a lattice mismatch higher than 4.6% has been seen to induce anisotropic nucleation and growth of Au−Cu nanostructures with highly strained surfaces,[51] the extended hydrogen bonds of DES serve as the soft template for the homogenous anisotropic growth of metallic nanostructures.[43,52] To validate this hypothesis, we performed a synthesis without adding the copper precursor in the reaction mixture, keeping all other conditions same. The reaction produced uniform gold nanostars (GNSs), as shown in Figure S1 (Supporting Information). This result, apart from revealing the soft-templating nature of the DES, indicates the requirement of Cu ions in reaction solution for the growth of highly branched flower-like nanostructures. Apart from anisotropic growth, the DES-mediated synthesis of metallic nanostructures has several other advantages over the common wet-chemical strategies. For example, the reactions take place in nonaqueous media, which require no additional surfactant or stabilizing agent. Moreover, using DES as the solvent and structure-directing agent, it is possible to fabricate metallic nanostructures of uniform morphologies with high yield.

Typical scanning electron microscopy (SEM) images of the Au−Cu nanostructures prepared at 1:0.5 molar ratios of Au and Cu are presented in Figure 1a−c, which reveal their uniform, flower-shaped nanostructure of similar size and shape. Morphological uniformity of the flower-shaped Au−Cu nanostructures is even clear in their low magnification transmission electron microscopy (TEM) images presented in Figure S2 (Supporting Information). Formation of branched structures of uniform morphology and 200−300 nm sizes in the sample is very clear in the high-magnification SEM image presented in Figure 1c. Because of the highly asymmetric shape of the branched nanostructures, they have a high surface area and interparticle void spaces or pores. Energy-dispersive spectroscopy (EDS) analysis revealed only the presence of
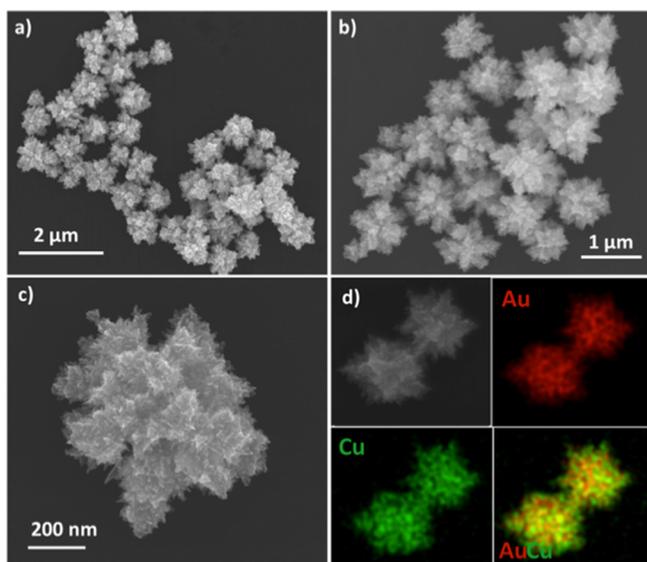
Figure 1. (a,b) Low and (c) high magnification SEM images, and (d) EDS-elemental mapping analysis of the flower-like bimetallic nanostructures fabricated with Au−Cu = 1:0.5 showing Au (red) and Cu (green) distribution, respectively.

Au and Cu in the nanostructures (Figure S3, Supporting Information). Furthermore, EDS-elemental mapping was performed on the nanostructures (Figure 1d), which indicates that Au and Cu atoms are uniformly distributed over the entire nanostructure. Notably, the overlapping image of Au and Cu elements also revealed that the bimetallic nanostructures mainly consist of Au and Cu atoms, apparently with slightly higher amount of Cu atoms at their surfaces. The EDS elemental line profiles recorded across the nanostructures (Figure 2) also revealed uniform distribution of Au and Cu in them. Intensities of the emission signal corresponding to the

two elements (Au and Cu) are also in accordance with their nominal concentrations in the reaction mixture. The results demonstrate that the formed nanostructures are Au−Cu bimetallic alloys.

To understand the mechanism of formation of Au−Cu bimetallic nanostructures in the DES, we monitored their growth kinetics by recording the UV−vis absorption spectra of the aliquots extracted from the reaction mixture at different time intervals (Figure S4, Supporting Information). As can be noticed in Figure S4 (Supporting Information), at t = 1 min, the absorption spectrum revealed a broad band extending from 520 to 900 nm, with a detectable hump around 550 nm. While the absorption spectrum extended over wide spectral range beyond the usual SPR band position of Au nanoparticles (around 520 nm) is the indication of bigger and highly dispersing nature of the formed nanostructures, the small hump detectable around 550 nm indicates they are rich in Au. In the spectrum recorded at t = 2 min, the absorption band remained broad, with a relative enhancement of intensity around 680 nm. While the intensity enhancement in the near-IR spectral range indicates the growth of the asymmetric nanostructures, evolution of the detectable absorption band around 680 nm indicates the incorporation of Cu in them. In fact, the SPR appearing around 650 nm for bimetallic Au−Cu nanostructures has also been detected by Hsia et al.[53] As the reaction proceeded further to t = 5, 10, and 15 min, the position of the 680 nm LSPR band remained around the same position, while its intensity decreased with time. The observed decrease in intensity for longer reaction time is due to increased incorporation of Cu in the nanostructures, causing the damping of the SPR peak of Au. The time evolution of the absorption spectra clearly indicates the formation of Au-rich nucleus or seed at the initial stage and subsequent simultaneous reduction of Cu^{2+} and Au^{3+} ions at the latter stage of the reaction, resulting the formation of bimetallic Au−Cu nanostructures.
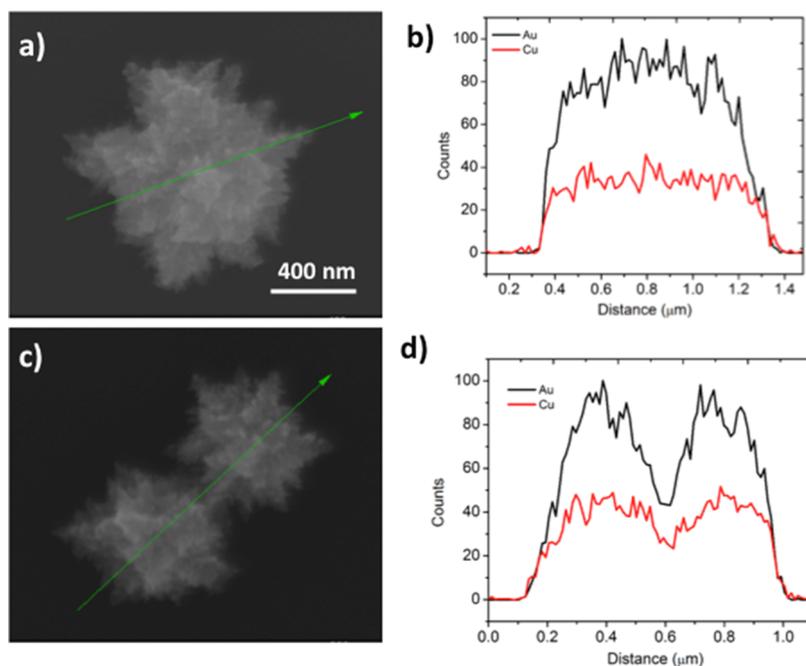

Figure 2. Typical SEM images and corresponding EDS line profiles of the Au−Cu nanostructures fabricated with Au−Cu = 1:0.5. As can be seen in (a,b) for a single nanostructure, and in (c,d) for two Au−Cu nanostructures, both Au and Cu are distributed homogeneously in the nanostructures.

The choline chloride and urea-derived DES contains a large amount of chlorine ions (Cl⁻). It is well known that the presence of halide ions (such as Br⁻, Cl⁻, I⁻ ions) in the reaction mixture significantly alters the reduction kinetics of metal ions, influencing the final morphology and elemental distribution of metallic nanostructures.[54] In the present synthesis, Cl⁻ ions play a key role in modulating the reduction rate of $HAuCl_4$ and $CuCl_2$ precursors. While the presence of Cl⁻ ions in high concentration enhances the reduction rate of both Au^{3+} and Cu^{2+} ions, the ratio of their reduction rate (i.e., the reduction rate of Au^{3+}: reduction rate of Cu^{2+}) becomes higher. As a result, initially, the Au^{3+} ions reduce at a little faster rate than Cu^{2+} ions, which is followed by the coreduction of Au^{3+} and Cu^{2+} in comparable reduction rate, leading to the formation of Au−Cu alloy nanostructures. In order to elucidate the role of DES as the soft template for the formation of flower-like particles, a control synthesis was performed by reducing the Au and Cu precursors in DI water (as solvent) without the assistance of DES under the same reaction conditions as used for DES-assisted synthesis described earlier. As can be observed in Figure S5 (Supporting Information), the resultant product consists highly agglomerated size-dispersed Au−Cu nanoparticles of varied morphologies, confirming the shape-directing role of DES. Furthermore, to understand the effect of the ChCl/urea ratio in the DES, we performed the same synthesis process in a DES prepared with ChCl and urea in 1:1 molar ratio. As can be observed in Figure S6 (Supporting Information), instead of flower-like morphology, the resulting nanostructures are anisotropic with concave surfaces. The difference in morphology between the nanostructures fabricated in DES with 1:2 and 1:1 molar ratios of ChCl and urea can be associated to the difference of Cl⁻ ion concentrations in the DES, which directly influences the surface energy of the initial seed particles affecting their growth kinetics. In fact, the reduction kinetics such as the reduction rate of metal precursors is seen to have a drastic influence on the final morphology of the metallic nanostructures.[55] To reveal the effect of reduction rate, we carried out two supporting experiments replacing AA by other reducing agents such as $NaBH_4$ (strong reducing agent) and D-glucose (mild-reducing agent). While the use of $NaBH_4$ as the reducing agent, as expected, produced agglomerated spherical nanoparticles (Figure S7, Supporting Information), use of D-glucose as the reducing agent produced nonuniform flower-like Au−Cu nanostructures with small Cu NPs adhered at the surface of Au nuclei (Figure S8, Supporting Information). These results clearly demonstrate the effect of reduction rate on the final morphology of the Au−Cu NSs.

To probe the influence of Cu^{2+} ion concentration in the reaction mixture on the final morphology of the nanostructures, we fabricated several samples at various Au and Cu precursor ratios (1:0.1, 1:0.2, 1:0.3, and 1:0.5). Figure 3 presents low- and high-magnification SEM images of the Au−Cu nanostructures fabricated with different Au and Cu precursor ratios. As can be noticed, the variation of Cu precursor concentration in the reaction mixture produces particles of different sizes and morphologies. While a low Cu concentration produced star-shaped Au−Cu nanostructures, higher Cu precursor concentration (e.g., Au−Cu = 1:0.5) produced flower-like Au−Cu nanostructures of uniform morphology. EDS elemental analysis of the Au−Cu NSs prepared at Au−Cu = 1:0.1 molar ratio (Figure S3, Supporting Information) revealed 87.71 at % of Au and 12.29 at % Cu in
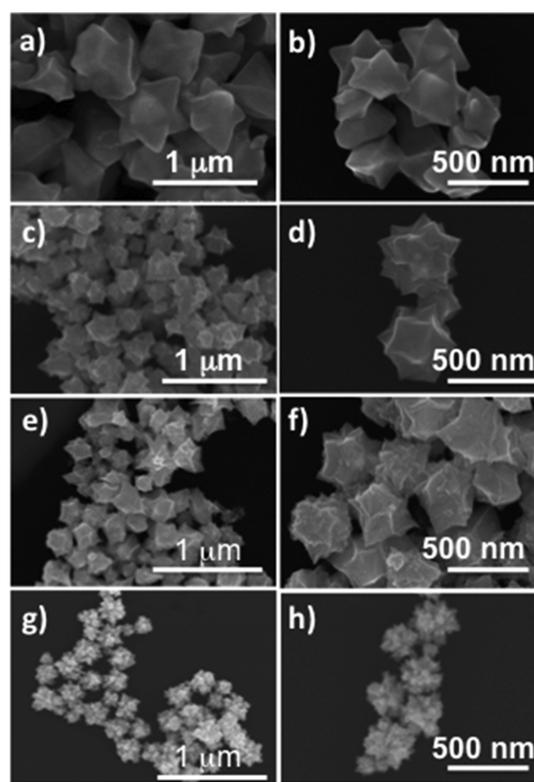

Figure 3. Representative low- and high-magnification SEM images of the Au−Cu nanostructures prepared at different Au and Cu molar ratios in the reaction solution: (a,b) Au−Cu = 1:0.1, (c,d) Au−Cu = 1:0.2, (e,f) Au−Cu = 1:0.3, and (g,h) Au−Cu = 1:0.5, respectively.

the sample, indicating that the ratio of the two elements in the final structures is close to their nominal molar ratio in the reaction mixture. Therefore, the nanostructures fabricated with different ratios of Au and Cu ions in the reaction mixtures were denoted by corresponding molar ratios.

The LSPR is one of the most important features of mono- and bi-metallic plasmonic nanostructures. Both the intensity and position of the LSPR band of the Au-based bimetallic nanoparticles depend strongly on their size and composition.[50] Hence, the optical properties of the fabricated Au−Cu NSs were studied by monitoring the variation of the LSPR peak position in their optical absorption spectra recorded in the UV−vis spectral range. Figure 4a displays the UV−vis absorption spectra of the as-grown Au−Cu nanostructures fabricated with different Cu precursor concentrations in the reaction mixture. While the pure Au nanostructures (Figure S9, Supporting Information) exhibited two characteristic SPR signals around 528 and broad peak at 645 nm, associated to their anisotropic shapes,[52] the NSs prepared with lowest Cu content (i.e., Au−Cu = 1:0.1) exhibited no clear LSPR band in its absorption spectrum with broad and intense absorption over the 500−850 nm spectral range, as has been observed for the nanostructures prepared with Au−Cu = 1:0.5 (Figure S4, Supporting Information) at the initial stage of reaction. As the concentration of Cu ions in the reaction mixture increased to Au/Cu = 1:0.3 & 1:0.5, there appeared two detectable LSPR bands around 610 and 741 nm. However, for higher Au/Cu ratio, as expected, the peak of 528 was red-shifted and a detectable LSPR band appeared around 748 nm, indicating the formation of Au−Cu alloy structures.[34,56] The redshift along with broadening of the SPR absorption peak with increasing
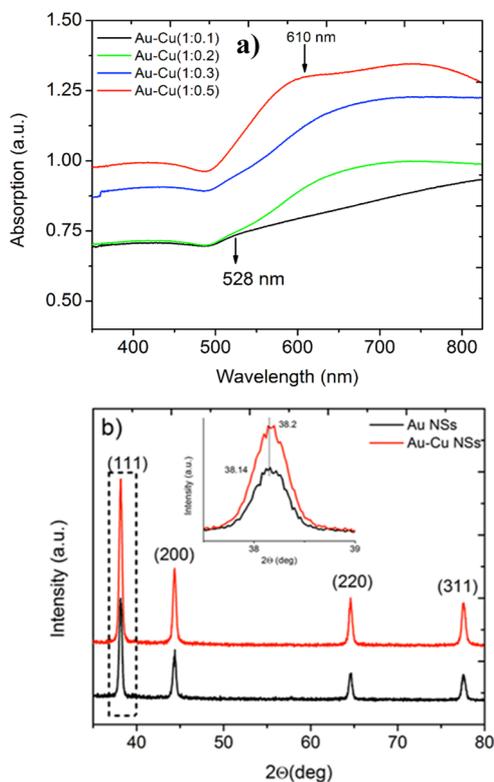
Figure 4. (a) UV−vis optical absorption spectra of the colloidal Au−Cu nanostructures prepared with different Au and Cu molar ratios; and (b) XRD patterns of Au−Cu nanostructures prepared at Au/Cu = 1:0.5, in comparison with pure Au nanostructures.

Cu content could be due to the incorporation of Cu causing the introduction of polycrystallinity, change in the dielectric constant of the material, and the variation in particle morphology.[57]

The structure of the as-synthesized Au−Cu nanostructures was analyzed further using the X-ray diffraction (XRD) technique. As can be seen in Figure 4b, in the 30−80° spectral range, the XRD pattern of the monometallic Au nanostructures revealed four diffraction peaks at around 38.18, 44.24, 64.63, and 77.54°, which correspond to the (111), (200), (220), and (311) planes of gold in the fcc phase.[52] On the other hand, the XRD pattern of the Au−Cu nanostructures revealed diffraction peaks associated to the (111), (200), (220), and (311) planes, slightly shifted toward the higher angle in comparison with their positions in Au NSs (JCPDF

no. 04-0784). The shift can be perceived better in the magnified XRD pattern presented as the inset of Figure 4b for the spectral region of the Au(111) diffraction band. Considering the Vegard's law,[58] observed shift of the diffraction band in the latter sample can be ascribed to the formation of Au−Cu bimetallic alloy in the nanostructures.[58] Minor broadening of the diffraction peaks of the bimetallic NSs probably occurs because of a reduction of crystallinity at the nanostructure surface. Bimetallic nature of the fabricated NSs was further verified by their X-ray photoelectron spectroscopy (XPS) analysis. The XPS survey spectrum of the sample (prepared at Au/Cu = 1:0.5) presented in Figure S10a (Supporting Information) confirms the presence of gold and copper elements in the sample and absence of any other element. The high-resolution XPS spectrum of the pristine Au NSs in the 4f core-level region (Figure S10b, Supporting Information) revealed components located at 83.9 and 87.5 eV. The binding energies (BE) correspond to the $4f_{7/2}$ and $4f_{5/2}$ orbitals of metallic Au (Au⁰).[59] Figure 5 presents the high-resolution XPS spectra of Au 4f and Cu 2P emissions of Au−Cu NSs. The Au 4f core level spectrum presented in Figure 5a revealed two components located at BE of 84.4 and 88.1 eV. As can be noticed, the position of the Au $4f_{7/2}$ and Au $4f_{5/2}$ emissions of Au−Cu NSs are at the higher energy side compared to their positions in pristine Au NSs, indicating the incorporation of Cu in the bimetallic NSs. On the other hand, there appeared two component bands for the Cu 2p emission (Figure 5b) at the BE positions 932.5 and 952.1 eV, which correspond to the Cu $2p_{3/2}$ and Cu $2p_{1/2}$ core-level emissions of metallic Cu, respectively.[59] The absence of strong satellite peaks around 935 and 955 eV confirmed that copper in the Au−Cu NSs does not exist in the Cu²⁺ state.[60]

2.2. SERS Activity of Au−Cu Nanostructures. In comparison to the isotropic structures, highly branched anisotropic metallic nanostructures exhibit greatly improved SERS performance because of their typical morphologies and presence of a large number of edges and cavities, which can provide intense "hot spots" with large electric-field enhancement.[20,22,61,62] To exploit the anisotropic shape of the Au−Cu nanostructures and their irregular surfaces, we further examined their utility as SERS substrates for molecular detection. To investigate the morphology and composition-dependent SERS activity, we carried out SERS measurements on the Au−Cu nanostructures fabricated with different Au/Cu ratios. All the SERS measurements were performed at room temperature, using a 633 nm He−Ne laser excitation under identical experimental conditions. CV was utilized as a model
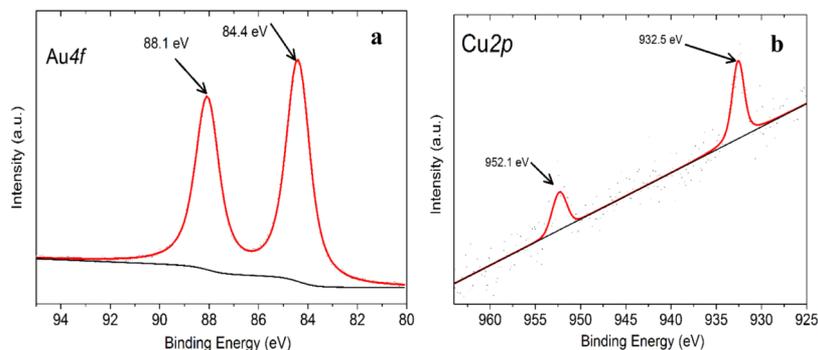

Figure 5. High-resolution XPS spectra in the (a) Au 4f and (b) Cu 2P core level regions of the as-synthesized Au−Cu (Au/Cu = 1:0.5) nanostructures.
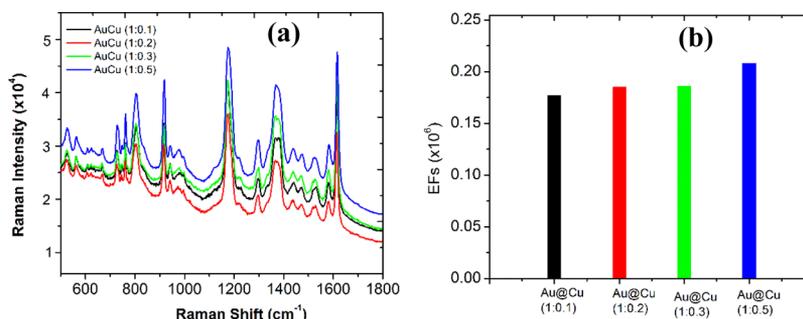
Figure 6. (a) SERS spectra of the CV solution (10 μL, 10^{-6} M) adsorbed over Au−Cu nanostructures of different compositions. (b) Histogram showing the SERS EFs for the Au−Cu nanostructures of different Cu contents.
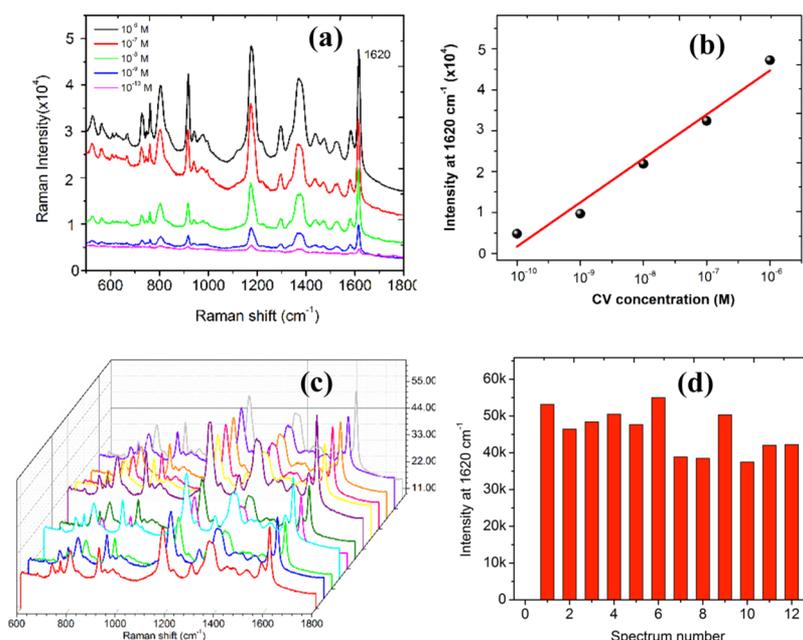

Figure 7. (a) SERS spectra recorded over the substrate fabricated with flower-like Au−Cu NSs for different (10^{-6} to 10^{-10} M) CV concentrations; (b) variation of 1620 cm^{-1} Raman band intensity as a function of CV concentration; (c) comparison of SERS spectra recorded at 12 different positions of the plasmonic substrate (fabricated with flower-like Au−Cu NSs) for CV solution of 10^{-6} M concentration; and (d) intensity variation of the 1620 cm^{-1} dispersion band recorded at 12 different random sites of a substrate fabricated with flower-like Au−Cu NSs.

analyte for SERS detection. The presence of sharp edges and pores in the fabricated Au−Cu nanostructures facilitates the adsorption of analyte molecules to detect them directly from their aqueous solutions. Therefore, we first recorded the SERS spectra in aqueous solutions of CV containing the same amounts of metallic nanostructures dispersed in them (Figure S11, Supporting Information). The SERS spectra of the Au−Cu nanostructures fabricated with different Au−Cu ratios were dispersed in 10^{-6} M CV solution. Intense and well-defined dispersion peaks appeared around 721, 803, 911, 1002, 1171, 1390, 1537, 1586, and 1620 cm^{-1} correspond to the characteristic vibrational bands of CV molecules.[63] As can be noticed in Figure S11 (Supporting Information), SERS signals from the samples containing lower Cu content are weaker in comparison to the signals recorded for the Au−Cu nanostructures containing higher Cu contents. Furthermore, we carried out substrate-based SERS measurements by depositing a fixed amount of nanostructures over silicon (Si) substrates. For that, first 50 μL (1.0 mg/mL) of colloidal Au−Cu nanostructures was dropcasted over a clean Si substrate and dried at ambient temperature. Following the same technique, SERS substrates were prepared using the nanostructures of

different Au−Cu ratios. The procedure adopted for preparing the substrates with different nanostructures has been presented in the Experimental Section. Figure 6a displays the SERS spectra of CV molecules recorded over SERS substrates fabricated using Au−Cu nanostructures of different Au−Cu ratios.

To quantify the SERS performance of the fabricated nanostructures, SERS enhancement factors (EFs) for Raman detection of CV molecules were estimated using the relation (eq 1)

$$EF = \frac{I_{SERS}}{N_{SERS}} \Big/ \frac{I_{Nor}}{N_{Nor}} \tag{1}$$

where I_{SERS} and I_{Nor} are the signal intensities of SERS and normal Raman spectra of CV for the same dispersion band (1620 cm^{-1} Raman band in the present case), and N_{SERS} and N_{Nor} represent the corresponding number of molecules in the focused incident laser spot. Assuming an uniform distribution of CV molecules over the substrates (nanostructures), the values of N_{SERS} and N_{Nor} in eq 1 can be substituted by the concentration of CV, that is, 1.0×10^{-6} and 1.0×10^{-3} M,

respectively, as the normal Raman spectra were recorded on CV solution of 1.0×10^{-3} M concentration (Figure S12, Supporting Information).

Figure 6b shows that the EF value for the nanostructures depends also on the Cu content in them. As can be noticed, all the samples revealed high CV signal, with highest EF ~ 0.21×10^6 for the substrate fabricated with flower-shaped Au−Cu nanostructures. The estimated EFs for the flower-shaped Au−Cu nanostructures were compared with some of the earlier reported values for the branched mono- and bimetallic nanostructures and presented Table S1 (Supporting Information). As can be seen, the flower-like Au−Cu nanostructure fabricated in this work exhibit higher or comparable SERS performance with respect to the SERS performance of asymmetric metallic nanostructures reported earlier. As the LSPR signal of Cu nanostructures is less intense in comparison to the same of Au nanostructures, apart from the difference in their positions (appear at higher wavelength for Cu nanostructures), the observed higher SERS signal enhancement by the flower-like Au−Cu nanostructures can be associated mainly to their special morphology, which provides intense SERS-active "hot spots" in their surface.

To evaluate the sensitivity of CV detection of the SERS substrates fabricated with flower-shaped Au−Cu nanostructures, which revealed highest EF, we recorded the SERS spectra of CV molecules over the particular substrate using CV solutions of different concentrations. Figure 7a depicts the SERS spectra of CV adsorbed over Au−Cu nanoflowers for CV concentrations from 10^{-6} to 10^{-10} M. As can be noticed in Figure 7b, the intensity of the 1620 cm^{-1} Raman signal increases almost linearly with the increase of CV concentration in the probe solution. Moreover, the Raman signal of the probe molecules is quite detectable for the CV concentration as low as 10^{-10} M. The sensitivity of the flower-shaped Au−Cu nanostructures exceeds or comparable with the previous studies of mono-/bimetallic branched nanostructures, which includes FeOOH-doped dendritic Ag nanostructures (10^{-10} M),[64] graphene/bilayers, silver/Cu hybrids (10^{-9} M),[65] porous Au−Ag alloy nanosphere arrays (10^{-10} M),[66] and hierarchical Au−CuO nanostructures (1.0×10^{-8} M).[67] As has been stated earlier, the enhanced SERS performance of the flower-shaped Au−Cu nanostructures can be mainly attributed to the presence of intense "hot spots" in large numbers over their porous branched surfaces. It must be noted that although the 633 nm excitation (He−Ne laser emission) utilized in the present study lie between the LSPR band positions of pure Au and Cu NSs, the excitation (laser radiation) could be effectively coupled with the LSPR emission of the bimetallic NSs, resulting in an enhancement of the SERS signal. Signal EFs estimated for the fabricated flower-like Au−Cu NSs are superior to the corresponding values reported for unbranched metallic nanostructures (see Table S1, Supporting Information).

As stability and reproducibility are the major concerns for practical applications of metal nanostructure-based SERS substrates, we also performed reproducibility tests on the SERS substrates fabricated with flower-like Au−Cu nanostructures (Au−Cu = 1:0.5). To demonstrate the reproducibility of the SERS substrate, we recorded SERS spectra at 12 random spots over the same substrate using a CV solution of 10^{-6} M concentration (Figure 7c). As can be noticed in Figure 7d, the intensity of the 1620 cm^{-1} Raman signal of CV recorded over 12 different spots varies between 40 and 60 K. The estimated

relative standard deviation (RSD) of the measured signal intensity was about 13.8%. RSD values less than that of 20% are considered to be acceptable for the SERS substrates for their practical applications.[68] Reproducibility and reliability of the fabricated SERS substrates were evaluated further by preparing six different SERS substrates using the same procedure and analyte solutions of a fixed concentration (10^{-6} M). The SERS spectra of the CV solution recorded over six different SERS substrates are shown in Figure S13 (Supporting Information). Estimated RSD of the SERS signal (1620 cm^{-1} band) recorded over six substrates was about 12.5 ± 0.7%, which indicates a good reproducibility of the fabricated substrates. The stability of the fabricated SERS substrates was probed further by performing SERS measurements under continuous laser irradiation at the same spot (Figure S14, Supporting Information). As can be observed, although the Raman signal (1620 cm^{-1}) intensity of the analyte (CV) molecules decreases gradually with the repeated irradiation of the probe laser beam, the signal is quite intense even after seven irradiation cycles at the same spot of the substrate. The observed decrease of Raman signal might be due to partial degradation of CV molecules. Overall, the obtained results indicate excellent performance (high sensitivity, reproducibility, and stability) of the SERS substrates fabricated using the flower-like Au−Cu nanostructures fabricated in DES.

3. CONCLUSIONS

In summary, we demonstrate a novel one-pot synthesis strategy for the fabrication of Au−Cu nanostructures of different compositions and tunable morphology, using a nonaqueous ChCl/urea-derived DES. Au−Cu nanostructures of different compositions could be obtained simply by varying the amount of the $CuCl_2$ precursor in the reaction mixture. Large lattice mismatch between the component elements and their distinct reduction potential in the Cl$^-$ ion-rich DES solvent are two key parameters which define the final morphology of the bimetallic nanostructures. Apart from morphology, the position of the LSPR bands of the bimetallic nanostructures can be effectively tuned from visible to the near infrared region, simply by changing the amount of Cu in Au−Cu NSs. Because of the special flower-like morphology and sharp edges, the nanostructures produce abundant intense "hot spots" under excitation of laser, which can enhance the Raman signals of analyte molecules (CV) significantly. Raman signal EF as high as 0.21×10^6 and CV detection sensitivity as low as 10^{-10} M were recorded for the SERS substrates fabricated using these flower-like Au−Cu nanostructures. The DES-mediated synthesis process utilized to fabricate anisotropic Au−Cu bimetallic nanostructures in this work can be adopted for the fabrication of other bimetallic nanostructures of different morphologies for their SERS-based spectroscopic applications.

4. EXPERIMENTAL SECTION

4.1. Chemicals and Materials. Choline chloride (ChCl, $(CH_3)_3N(Cl)CH_2CH_2OH]Cl$), urea ($CO(NH_2)_2$), chloroauric acid ($HAuCl_4 \cdot 4H_2O$, 99.9%), and AA (99%) were purchased from Sigma-Aldrich, Mexico. All the chemicals were utilized as received. Deionized (DI) water from a Millipore system was utilized both for cleaning the used glassware and the nanostructures.

4.2. Preparation of ChCl/Urea-Based DES. Prior to preparation of DES, the ChCl was heated at 90 °C for 2 h to eliminate its moisture content, if any. The ChCl/urea-based DES was prepared following the previous report.[52] Briefly, ChCl and urea were mixed together in a 1:2 molar ratio and heated at 80 °C until a transparent colorless liquid mixture is obtained. The DES fabricated this way was cooled down to room temperature and kept at this temperature for at least 2 h prior to its use in nanostructure synthesis.

4.3. Synthesis of Au−Cu Nanostructures. For the synthesis of Au−Cu nanostructures, 10 mg of $HAuCl_4 \cdot 4H_2O$ and 5 mg of $CuCl_2$ were added to 20 mL of freshly prepared DES in a glass beaker under magnetic stirring at 60 °C, until obtaining a homogeneous dispersion. Separately, another solution was prepared by mixing DES and AA by adding 50 mg of AA in 10 mL of DES under magnetic stirring at 60 °C. Then, the second solution (AA containing DES) was quickly added to the earlier metal precursor containing mixture solution under magnetic stirring, keeping the temperature of the mixture fixed at 60 °C. The mixture solution-containing beaker was covered with aluminum foil to avoid the absorption of moisture from the ambient. The color of the reaction mixture slowly turned brown from yellow within 5 min. The reaction was continued for 30 min. After that, an equal volume (30 mL) of DI water was added to the reaction mixture. The formed nanostructures were separated from the colloidal solution by centrifugation at 12,000 rpm and washed with DI water four times to eliminate DES and unreacted precursors (if any) from their surfaces. Au@Cu nanostructures of different nominal Au and Cu molar ratios were fabricated using an identical procedure, only by changing the molar ratio of Au and Cu precursors (1:0.1, 1:0.2, 1:0.3, and 1:0.5) in the precursor solution.

4.4. Characterization of Au−Cu Nanostructures. A JEOL-JSM7401F field emission scanning electron microscope operating at 20 kV and a JEOL JEM-1010 transmission electron microscope operating at 80 kV accelerating voltage were utilized to study the morphology and structure of the fabricated nanostructures. Distributions of Au and Cu in the nanostructures were investigated through their EDS mapping in a Hitachi SU 8020 scanning electron microscope. Powder XRD spectra of the samples were collected in a Rigaku Ultima IV X-ray diffractometer, using Cu Kα radiation (λ = 1.0654 Å). XPS analysis of the nanostructures was performed in an Intercovamex-XPS110 (Intercovamex, Mexico) spectrometer, using nonmonochromatic Al Kα (1486.7 eV) X-ray source. All the recorded XPS spectra were corrected utilizing the C 1s line at 284.8 eV. Room temperature optical absorption spectra of the colloidal nanostructures were recorded in the 300−1100 nm spectral range, in an Agilent 8453 UV−vis spectrophotometer, utilizing plastic cuvettes of 1 cm path length. Raman and SERS spectra of the samples were collected in a Bruker (SENTERRA) Raman spectrometer, using the 633 nm line of a He−Ne laser as the excitation source.

4.5. SERS Study of the Au−Cu Nanostructures. For the study of solution-based SERS performance of the fabricated nanostructures, first, a fixed amount of the as-prepared Au−Cu colloidal sample (1.0 mg/mL in DI water) was incubated with 25 μL of aqueous CV solution (10^{-6} M) for 2 h. Then, the CV-adsorbed nanostructures were separated from the CV solution by centrifugation and redispersed in DI water. The CV-adsorbed colloidal nanostructures were then transferred to a glass cuvette for the SERS measurements. On the other hand,

for the SERS study over silicon substrates, a 50 μL of colloidal Au−Cu sample (1.0 mg/mL in DI water) was dropcasted over clean silicon wafers (8 mm × 8 mm) and dried in air. After that, 25 μL of an aqueous CV solution (10^{-6} M) was dropped over the sample and dried under ambiental conditions. The CV deposited substrate was then washed with DI water twice to remove unabsorbed CV molecules from the nanostructures and dried further under ambiental conditions. For reference, a SERS substrate was prepared by dropcasting the CV solution (25 μL) over the silicon substrate without prior deposition of metal nanostructures. Both the Raman and SERS spectra were collected in a Bruker (SENTERRA) Raman spectrometer, using a laser (He−Ne) excitation wavelength of 633 nm of 2.7 mW. The diameter of the exciting laser spot was fixed to 4.7 μm under a 50× lens, and the signal acquisition time was fixed to 3 s.

■ ASSOCIATED CONTENT

ⓢ Supporting Information
The Supporting Information is available free of charge at https://pubs.acs.org/doi/10.1021/acsomega.9b04355.

> TEM images, EDS elemental analysis of Au−Cu NSs, XPS survey spectra, SERS spectra of reproducibility, and stability analysis (PDF)

■ AUTHOR INFORMATION

Corresponding Authors
Siva Kumar-Krishnan − *CONACYT-Instituto de Física, Benemérita Universidad Autónoma de Puebla, Puebla 72570, Mexico;* ⓞ orcid.org/0000-0002-9672-9335; Email: sivakumar@ifuap.buap.mx

Umapada Pal − *Instituto de Física, Benemérita Universidad Autónoma de Puebla, Puebla 72570, Mexico;* ⓞ orcid.org/0000-0002-5665-106X; Email: upal@ifuap.buap.mx

Author
Rodrigo Esparza − *Centro de Física Aplicada y Tecnología Avanzada, Universidad Nacional Autónoma de México, Santiago de Querétaro, Querétaro 76230, Mexico*

Complete contact information is available at:
https://pubs.acs.org/10.1021/acsomega.9b04355

Notes
The authors declare no competing financial interest.

■ ACKNOWLEDGMENTS

■ REFERENCES

(1) Jiang, N.; Zhuo, X.; Wang, J. Active Plasmonics: Principles, Structures, and Applications. *Chem. Rev.* **2018**, *118*, 3054−3099.

(2) Kauranen, M.; Zayats, A. V. Nonlinear Plasmonics. *Nat. Photonics* **2012**, *6*, 737−748.

(3) Xie, J.; Lee, S.; Chen, X. Nanoparticle-Based Theranostic Agents. *Adv. Drug Delivery Rev.* **2010**, *62*, 1064−1079.

(4) Atwater, H. A.; Polman, A. Plasmonics for Improved Photovoltaic Devices. *Nat. Mater.* **2010**, *9*, 205−213.

(5) Anker, J. N.; Hall, W. P.; Lyandres, O.; Shah, N. C.; Zhao, J.; Van Duyne, R. P. Biosensing with Plasmonic Nanosensors. *Nat. Mater.* **2008**, *7*, 442−453.

(6) Rodríguez-Lorenzo, L.; de la Rica, R.; Álvarez-Puebla, R. a.; Liz-Marzán, L. M.; Stevens, M. M. Plasmonic Nanosensors with Inverse Sensitivity by Means of Enzyme-Guided Crystal Growth. *Nat. Mater.* **2012**, *11*, 604−607.

(7) Aslam, U.; Chavez, S.; Linic, S. Controlling Energy Flow in Multimetallic Nanostructures for Plasmonic Catalysis. *Nat. Nanotechnol.* **2017**, *12*, 1000−1005.

(8) Aberasturi, D. J. De; Serrano-montes, A. B.; Liz-marzán, L. M. Modern Applications of Plasmonic Nanoparticles : From Energy to Health. *Adv. Opt. Mater.* **2015**, *3*, 602.

(9) Howes, P. D.; Rana, S.; Stevens, M. M. Plasmonic Nanomaterials for Biodiagnostics. *Chem. Soc. Rev.* **2014**, *43*, 3835−3853.

(10) Matricardi, C.; Hanske, C.; Garcia-pomar, J. L.; Langer, J.; Mihi, A.; Liz-Marzán, L. M. Gold Nanoparticle Plasmonic Superlattices as Surface-Enhanced Raman Spectroscopy Substrates. *ACS Nano* **2018**, *12*, 8531−8539.

(11) Lin, L.; Zhang, Q.; Li, X.; Qiu, M.; Jiang, X.; Jin, W.; Gu, H.; Lei, D. Y.; Ye, J. Electron Transport Across Plasmonic Molecular Nanogaps Interrogated with Surface-Enhanced Raman Scattering. *ACS Nano* **2018**, *12*, 6492−6503.

(12) Lombardi, A.; Demetriadou, A.; Weller, L.; Andrae, P.; Benz, F.; Chikkaraddy, R.; Aizpurua, J.; Baumberg, J. J. Anomalous Spectral Shift of Near- and Far-Field Plasmonic Resonances in Nanogaps. *ACS Photonics* **2016**, *3*, 471−477.

(13) Rycenga, M.; Cobley, C. M.; Zeng, J.; Li, W.; Moran, C. H.; Zhang, Q.; Qin, D.; Xia, Y. Controlling the Synthesis and Assembly of Silver Nanostructures for Plasmonic Applications. *Chem. Rev.* **2011**, *111*, 3669−3712.

(14) Li, C.-Y.; Meng, M.; Huang, S.-C.; Li, L.; Huang, S.-R.; Chen, S.; Meng, L.-Y.; Panneerselvam, R.; Zhang, S.-J.; Ren, B.; Yang, Z.-L.; Li, J.-F.; Tian, Z.-Q. "Smart" Ag Nanostructures for Plasmon-Enhanced Spectroscopies. *J. Am. Chem. Soc.* **2015**, *137*, 13784−13787.

(15) Yang, X.; Yang, M.; Pang, B.; Vara, M.; Xia, Y.; States, U. Gold Nanomaterials at Work in Biomedicine. *Chem. Rev.* **2015**, *115*, 10410−10488.

(16) Pastoriza-Santos, I.; Sánchez-Iglesias, A.; Rodríguez-González, B.; Liz-Marzán, L. M. Aerobic Synthesis of Cu Nanoplates with Intense Plasmon Resonances. *Small* **2009**, *5*, 440−443.

(17) Dai, L.; Song, L.; Huang, Y.; Zhang, L.; Lu, X.; Zhang, J.; Chen, T. Bimetallic Au/Ag Core-Shell Superstructures with Tunable Surface Plasmon Resonance in the Near-Infrared Region and High Performance Surface-Enhanced Raman Scattering. *Langmuir* **2017**, *33*, 5378−5384.

(18) Liu, K.; Bai, Y.; Zhang, L.; Yang, Z.; Fan, Q.; Zheng, H.; Yin, Y.; Gao, C. Porous Au–Ag Nanospheres with High-Density and Highly Accessible Hotspots for SERS Analysis. *Nano Lett.* **2016**, *16*, 3675−3681.

(19) Chew, W. S.; Pedireddy, S.; Lee, Y. H.; Tjiu, W. W.; Liu, Y.; Yang, Z.; Ling, X. Y. Nanoporous Gold Nanoframes with Minimalistic Architectures: Lower Porosity Generates Stronger Surface-Enhanced Raman Scattering Capabilities. *Chem. Mater.* **2015**, *27*, 7827−7834.

(20) Wang, L.; Li, H.; Tian, J.; Sun, X. Monodisperse, Micrometer-Scale, Highly Crystalline, Nanotextured Ag Dendrites: Rapid, Large-Scale, Wet-Chemical Synthesis and Their Application as SERS Substrates. *ACS Appl. Mater. Interfaces* **2010**, *2*, 2987−2991.

(21) Yin, H. J.; Chen, Z. Y.; Zhao, Y. M.; Lv, M. Y.; Shi, C. A.; Wu, Z. L.; Zhang, X.; Liu, L.; Wang, M. L.; Xu, H. J. Ag@Au Core-Shell Dendrites: A Stable, Reusable and Sensitive Surface Enhanced Raman Scattering Substrate. *Sci. Rep.* **2015**, *5*, 14502.

(22) Yüksel, S.; Ziegler, M.; Goerke, S.; Huebner, U.; Weber, K.; Schaaf, P.; Meyer, H.-G.; Cialla-May, D.; Popp, J. Hierarchically-Designed 3D Flower-Like Composite Nanostructures as an Ultrastable, Reproducible, and Sensitive SERS Substrate. *ACS Appl. Mater. Interfaces* **2017**, *9*, 38854−38862.

(23) Liu, S.-Y.; Tian, X.-D.; Zhang, Y.; Li, J.-F. Quantitative Surface-Enhanced Raman Spectroscopy through the Interface-Assisted Self-Assembly of Three-Dimensional Silver Nanorod Substrates. *Anal. Chem.* **2018**, *90*, 7275.

(24) Nam, J.-M.; Oh, J.-W.; Lee, H.; Suh, Y. D. Plasmonic Nanogap-Enhanced Raman Scattering with Nanoparticles. *Acc. Chem. Res.* **2016**, *49*, 2746−2755.

(25) Pradhan, M.; Sinha, A. K.; Pal, T. Redox Transformation Reaction for Hierarchical Hollow Au−MnOOH Flowers for High SERS Activity. *RSC Adv.* **2014**, *4*, 30315−30324.

(26) Jin, Q.; Li, M.; Polat, B.; Paidi, S. K.; Dai, A.; Zhang, A.; Pagaduan, J. V.; Barman, I.; Gracias, D. H. Mechanical Trap Surface-Enhanced Raman Spectroscopy for Three-Dimensional Surface Molecular Imaging of Single Live Cells. *Angew. Chem., Int. Ed.* **2017**, *56*, 3822−3826.

(27) Nehl, C. L.; Liao, H.; Hafner, J. H. Optical Properties of Star-Shaped Gold Nanoparticles. *Nano Lett.* **2006**, *6*, 683−688.

(28) Fang, J.; Du, S.; Lebedkin, S.; Li, Z.; Kruk, R.; Kappes, M.; Hahn, H. Gold Mesostructures with Tailored Surface Topography and Their Self-Assembly Arrays for Surface-Enhanced Raman Spectroscopy. *Nano Lett.* **2010**, *10*, 5006−5013.

(29) Niu, W.; Chua, Y. A. A.; Zhang, W.; Huang, H.; Lu, X. Highly Symmetric Gold Nanostars: Crystallographic Control and Surface-Enhanced Raman Scattering Property. *J. Am. Chem. Soc.* **2015**, *137*, 10460−10463.

(30) Motl, N. E.; Ewusi-Annan, E.; Sines, I. T.; Jensen, L.; Schaak, R. E. Au-Cu Alloy Nanoparticles with Tunable Compositions and Plasmonic Properties: Experimental Determination of Composition and Correlation with Theory. *J. Phys. Chem. C* **2010**, *114*, 19263−19269.

(31) Guisbiers, G.; Mejia-Rosales, S.; Khanal, S.; Ruiz-Zepeda, F.; Whetten, R. L.; José-Yacaman, M. Gold-Copper Nano-Alloy, " Tumbaga ", in the Era of Nano: Phase Diagram and Segregation. *Nano Lett.* **2014**, *14*, 6718−6726.

(32) Zhu, W.; Zhang, L.; Yang, P.; Hu, C.; Dong, H.; Zhao, Z.-J.; Mu, R.; Gong, J. Formation of Enriched Vacancies for Enhanced CO_2 Electrocatalytic Reduction over AuCu Alloys. *ACS Energy Lett.* **2018**, *3*, 2144−2149.

(33) He, R.; Wang, Y.-C.; Wang, X.; Wang, Z.; Liu, G.; Zhou, W.; Wen, L.; Li, Q.; Wang, X.; Chen, X.; Zeng, J.; Hou, J. G. Facile Synthesis of Pentacle Gold-Copper Alloy Nanocrystals and Their Plasmonic and Catalytic Properties. *Nat. Commun.* **2014**, *5*, 4327.

(34) Kim, D.; Resasco, J.; Yu, Y.; Asiri, A. M.; Yang, P. Synergistic Geometric and Electronic Effects for Electrochemical Reduction of Carbon Dioxide Using Gold-Copper Bimetallic Nanoparticles. *Nat. Commun.* **2014**, *5*, 4948.

(35) Yin, J.; Shan, S.; Yang, L.; Mott, D.; Malis, O.; Petkov, V.; Cai, F.; Shan Ng, M.; Luo, J.; Chen, B. H.; Engelhard, M.; Zhong, C.-J. Gold-Copper Nanoparticles: Nanostructural Evolution and Bifunctional Catalytic Sites. *Chem. Mater.* **2012**, *24*, 4662−4674.

(36) Thota, S.; Wang, Y.; Zhao, J. Colloidal Au−Cu Alloy Nanoparticles: Synthesis, Optical Properties and Applications. *Mater. Chem. Front.* **2018**, *2*, 1074−1089.

(37) Chen, W.; Yu, R.; Li, L.; Wang, A.; Peng, Q.; Li, Y. A Seed-Based Diffusion Route to Monodisperse Intermetallic CuAu Nanocrystals. *Angew. Chem., Int. Ed.* **2010**, *49*, 2917−2921.

(38) He, R.; Wang, Y. C.; Wang, X.; Wang, Z.; Liu, G.; Zhou, W.; Wen, L.; Li, Q.; Wang, X.; Chen, X.; Zeng, J.; Hou, J. G. Facile Synthesis of Pentacle Gold-Copper Alloy Nanocrystals and Their Plasmonic and Catalytic Properties. *Nat. Commun.* **2014**, *5*, 4327.

(39) Liu, Y.; Walker, A. R. H. Monodisperse Gold-Copper Bimetallic Nanocubes: Facile One-Step Synthesis with Controllable Size and Composition. *Angew. Chem., Int. Ed.* **2010**, *49*, 6781−6785.

(40) Wagle, D. V.; Zhao, H.; Baker, G. a. Deep Eutectic Solvents: Sustainable Media for Nanoscale and Functional Materials. *Acc. Chem. Res.* **2014**, *47*, 2299−2308.

(41) Abbott, A. P.; Boothby, D.; Capper, G.; Davies, D. L.; Rasheed, R. K. Deep Eutectic Solvents Formed between Choline Chloride and Carboxylic Acids: Versatile Alternatives to Ionic Liquids. *J. Am. Chem. Soc.* **2004**, *126*, 9142.

(42) Zhang, Q.; De Oliveira Vigier, K.; Royer, S.; Jérôme, F. Deep Eutectic Solvents: Syntheses, Properties and Applications. *Chem. Soc. Rev.* **2012**, *41*, 7108−7146.

(43) Zhang, J.; Wu, T.; Chen, S.; Feng, P.; Bu, X. Versatile Structure-Directing Roles of Deep-Eutectic Solvents and Their Implication in the Generation of Porosity and Open Metal Sites for Gas Storage. *Angew. Chem., Int. Ed.* **2009**, *48*, 3486−3490.

(44) Liao, H.-G.; Jiang, Y.-X.; Zhou, Z.-Y.; Chen, S.-P.; Sun, S.-G. Shape-Controlled Synthesis of Gold Nanoparticles in Deep Eutectic Solvents for Studies of Structure-Functionality Relationships in Electrocatalysis. *Angew. Chem.* **2008**, *120*, 9240−9243.

(45) Adhikari, L.; Larm, N. E.; Baker, G. A. Argentous Deep Eutectic Solvent Approach for Scaling up the Production of Colloidal Silver Nanocrystals. *ACS Sustainable Chem. Eng.* **2019**, *7*, 11036−11043.

(46) Karimi, M.; Eshraghi, M. J. One-Pot and Green Synthesis of Mn_3O_4 nanoparticles Using an All-in-One System (Solvent, Reactant and Template) Based on Ethaline Deep Eutectic Solvent. *J. Alloys Compd.* **2017**, *696*, 171−176.

(47) Thorat, G. M.; Jadhav, H. S.; Roy, A.; Chung, W.-J.; Seo, J. G. Dual Role of Deep Eutectic Solvent as a Solvent and Template for the Synthesis of Octahedral Cobalt Vanadate for an Oxygen Evolution Reaction. *ACS Sustainable Chem. Eng.* **2018**, *6*, 16255−16266.

(48) Chen, F.; Xie, S.; Zhang, J.; Liu, R. Synthesis of Spherical Fe_3O_4 magnetic Nanoparticles by Co-Precipitation in Choline Chloride/urea Deep Eutectic Solvent. *Mater. Lett.* **2013**, *112*, 177−179.

(49) Boston, R.; Foeller, P. Y.; Sinclair, D. C.; Reaney, I. M. Synthesis of Barium Titanate Using Deep Eutectic Solvents. *Inorg. Chem.* **2017**, *56*, 542−547.

(50) Alvarez-paneque, A. F.; Rodríguez-González, B.; Pastoriza-santos, I.; Liz-Marzán, L. M. Shape-Templated Growth of Au@Cu Nanoparticles. *J. Phys. Chem. C* **2013**, *117*, 2474−2479.

(51) Meng, M.; Fang, Z.; Zhang, C.; Su, H.; He, R.; Zhang, R.; Li, H.; Li, Z.-Y.; Wu, X.; Ma, C.; Zeng, J. Integration of Kinetic Control and Lattice Mismatch To Synthesize Pd@AuCu Core−Shell Planar Tetrapods with Size-Dependent Optical Properties. *Nano Lett.* **2016**, *16*, 3036−3041.

(52) Kumar-Krishnan, S.; Prokhorov, E.; Arias de Fuentes, O.; Ramírez, M.; Bogdanchikova, N.; Sanchez, I. C.; Mota-Morales, J. D.; Luna-Bárcenas, G. Temperature-Induced Au Nanostructure Synthesis in a Nonaqueous Deep-Eutectic Solvent for High Performance Electrocatalysis. *J. Mater. Chem. A* **2015**, *3*, 15869−15875.

(53) Hsia, C.-F.; Madasu, M.; Huang, M. H. Aqueous Phase Synthesis of Au-Cu Core-Shell Nanocubes and Octahedra with Tunable Sizes and Noncentrally Located Cores. *Chem. Mater.* **2016**, *28*, 3073−3079.

(54) Hsu, S.-C.; Chuang, Y.-C.; Sneed, B. T.; Cullen, D. A.; Chiu, T.-W.; Kuo, C.-H. Turning the Halide Switch in the Synthesis of Au-Pd Alloy and Core-Shell Nanoicosahedra with Terraced Shells: Performance in Electrochemical and Plasmon-Enhanced Catalysis. *Nano Lett.* **2016**, *16*, 5514−5520.

(55) Yang, T.-H.; Gilroy, K. D.; Xia, Y. Reduction Rate as a Quantitative Knob for Achieving Deterministic Synthesis of Colloidal Metal Nanocrystals. *Chem. Sci.* **2017**, *8*, 6730−6749.

(56) Xu, Z.; Lai, E.; Shao-Horn, Y.; Hamad-Schifferli, K. Compositional Dependence of the Stability of AuCu Alloy Nano-particles. *Chem. Commun.* **2012**, *48*, 5626−5628.

(57) Bryant, G. W.; Garcı, F. J. Mapping the Plasmon Resonances of Metallic Nanoantennas. *Nano Lett.* **2008**, *8*, 631−636.

(58) Wang, N.; Han, Y.; Xu, Y.; Gao, C.; Cao, X. Detection of H_2O_2 at the Nanomolar Level by Electrode Modified with Ultrathin AuCu Nanowires. *Anal. Chem.* **2015**, *87*, 457−463.

(59) Van Thuan, D.; Tri Khoa, N.; Kim, S. W.; Kim, E. J.; Hahn, S. H. Morphology-Dependent Selective Hydrogenation Catalysis of Hollow AuCu Bimetallic Nanostructures. *J. Catal.* **2015**, *329*, 144−150.

(60) Gowthaman, N. S. K.; Shankar, S.; Abraham John, S. Substrate Catalyzed Formation of Au-Cu Bimetallic Nanoparticles as Electro-catalyst for the Reduction of Dioxygen and Hydrogen Peroxide. *J. Electroanal. Chem.* **2018**, *812*, 37−44.

(61) Nabeela, K.; Thomas, R. T.; Nair, J. B.; Maiti, K. K.; Warrier, K. G. K.; Pillai, S. TEMPO-Oxidized Nanocellulose Fiber-Directed Stable Aqueous Suspension of Plasmonic Flower-like Silver Nano-

constructs for Ultra-Trace Detection of Analytes. *ACS Appl. Mater. Interfaces* **2016**, *8*, 29242−29251.

(62) Reguera, J.; Langer, J.; Jiménez de Aberasturi, D.; Liz-Marzán, L. M.; Langer, J. Anisotropic Metal Nanoparticles for Surface Enhanced Raman Scattering. *Chem. Soc. Rev.* **2017**, *46*, 3866−3885.

(63) Kumar-Krishnan, S.; Estevez-González, M.; Pérez, R.; Esparza, R.; Meyyappan, M. A General Seed-Mediated Approach to the Synthesis of AgM (M = Au, Pt, and Pd) Core−shell Nanoplates and Their SERS Properties. *RSC Adv.* **2017**, *7*, 27170−27176.

(64) Pradhan, M.; Maji, S.; Sinha, A. K.; Dutta, S.; Pal, T. Sensing Trace Arsenate by Surface Enhanced Raman Scattering Using a FeOOH Doped Dendritic Ag Nanostructure. *J. Mater. Chem. A* **2015**, *3*, 10254−10257.

(65) Zhang, M.; Zheng, Z.; Liu, H.; Wang, D.; Chen, T.; Liu, J.; Wu, Y. Rationally Designed Graphene/Bilayer Silver/Cu Hybrid Structure with Improved Sensitivity and Stability for Highly Efficient SERS Sensing. *ACS Omega* **2018**, *3*, 5761−5770.

(66) Zhang, T.; Sun, Y.; Hang, L.; Li, H.; Liu, G.; Zhang, X.; Lyu, X.; Cai, W.; Li, Y. Periodic Porous Alloyed Au-Ag Nanosphere Arrays and Their Highly Sensitive SERS Performance with Good Reproducibility and High Density of Hotspots. *ACS Appl. Mater. Interfaces* **2018**, *10*, 9792−9801.

(67) Pal, J.; Ganguly, M.; Dutta, S.; Mondal, C.; Negishi, Y.; Pal, T. Hierarchical Au−CuO Nanocomposite from Redox Transformation Reaction for Surface Enhanced Raman Scattering and Clock Reaction. *CrystEngComm* **2014**, *16*, 883−893.

(68) Natan, M. J. Concluding Remarks: Surface Enhanced Raman Scattering. *Faraday Discuss.* **2006**, *132*, 321−328.